Macromolecules
ARTICLE
pubs.acs.org/Macromolecules

Dynamics of Crystallization and Disorder during Annealing of P3HT/PCBM Bulk Heterojunctions

Samuele Lilliu,*,† Tiziano Agostinelli,‡ Ellis Pires,† Mark Hampton,† Jenny Nelson,‡ and J. Emyr Macdonald†

†School of Physics and Astronomy, Cardiff University, Queens Buildings, The Parade, Cardiff CF243AA, United Kingdom

‡Department of Physics and Centre for Plastic Electronics, Blackett Laboratory, Imperial College London, Prince Consort Road, London SW7 2BW, United Kingdom

S *Supporting Information*

ABSTRACT: A real-time crystallographic analysis of P3HT/PCBM films during thermal annealing is reported, detailing the temporal variation of crystallization, disorder, and orientational spread during the annealing. Five P3HT/PCBM chlorobenzene solutions with different P3HT concentrations (0, 33, 50, 67, 100 wt %) were spin coated on SiO_2 substrates. The thick films (∼100 nm) were studied during annealing (50 min at 140 °C), with in situ synchrotron grazing incidence X-ray diffraction (GI-XRD) and a sampling time <8 s. For the first time, the evolution of the crystal structure is analyzed taking into account P3HT paracrystallinity. The following were observed: a predominance of edge-on P3HT lamellae in the as-spun and annealed films; changes in concentration-dependent edge-on lamellar orientation spread along the alkyl-stacking direction and paracrystalline disorder after annealing; a permanent lamellar stretching just along the alky-stacking direction after annealing; an increase in the P3HT domain size along only the alkyl-stacking direction for the edge-on lamellae, with dynamics consistent with PCBM acting as a plasticizer for P3HT; and finally, an increase in the PCBM concentration at the sample−air interface. We show that the paracrystalline correction is important to calculate correctly the domain size as deduced from GI-XRD.

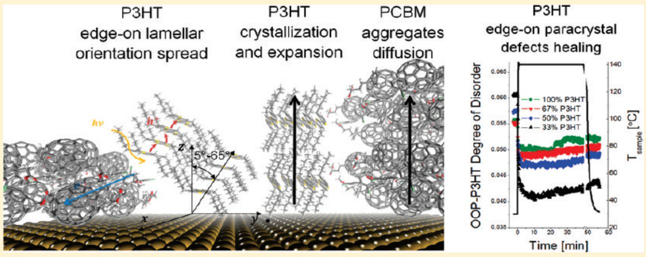

INTRODUCTION

Since the past decade, low-cost solution-processable organic photovoltaics (OPVs), based on bulk heterojunction (BHJ) architectures have experienced a continuous evolution.[1] Despite being outperformed by other material systems,[2] the donor−acceptor blend of regioregular poly(3-hexylthiophene) (rr-P3HT) and phenyl-C_{61}-butyric acid methyl ester (PCBM), remains fundamental as an OPV benchmark.

Kayunkid et al.[3] recently reported that P3HT crystallizes with a monoclinic (a = 16 to 17 Å (depending on the processing conditions), b = 7.8 Å, c = 7.8 Å, γ = 86.5°) unit cell, with space group $P2_1/c$ and with two chains per cell. P3HT self-organizes into lamellar structures.[4] A lamella is made of stacked backbones in the direction of the alkyl side chains (**a** direction, Figure 1a−c). In turn adjacent lamellae are stacked (stacking distance = $b/2$) perpendicular to the parallel/cofacial conjugated backbones (**b** direction, Figure 1a−c). In a schematic view, the π-stacking direction is always orthogonal to the alkyl-stacking direction and can be parallel to the sample substrate, with the alkyl-stacking direction perpendicular (edge-on, Figure 1a) to the sample substrate or with the alkyl-stacking direction parallel to the sample substrate (face-on, b). The arrangement with the backbone perpendicular to the substrate, with both the π-stacking and alkyl-stacking directions parallel to the substrate, is far less likely, being reported only in nanoimprinted samples[4e,f] (Figure 1c). Processing conditions,[5] solvent,[6] molecular weight,[4b,5a,6b] and substrate treatment[7] can affect the lamellar orientation and domain size. P3HT nanoscale mobility is highly anisotropic: hole (h^+) charge mobility is greatest in the backbone direction, lower in the π-stacking direction (conduction by hopping) and negligible in the alkyl direction.[8] The vertical structure, with the P3HT chain backbones perpendicular to the sample substrate, would be desirable in OPVs[9] because this would ensure high charge mobility pathways for the photogenerated charges to travel along their respective electrodes. Furthermore, conduction can occur via mesoscale hopping through polymer chains bridges[1c] between crystalline domains,[1b] forming percolation pathways along the vertical structure. In reality, P3HT films show a complex phasic structure, where crystalline domains are surrounded by a significant amount of amorphous P3HT.[5a,7,10] Moreover different backbones coexist in the all-trans and gauche forms.[11]

PCBM, in the model proposed by Rispens et al.,[12] crystallizes from chlorobenzene with a triclinic (a = 13.83 Å, b = 15.29 Å, c = 19.25 Å, α = 80.26°, β = 78.56°, γ = 80.41°) unit cell (Figure 1d), and does not preferentially orientate with respect to the sample

Received: December 10, 2010
Revised: February 10, 2011
Published: March 16, 2011

dx.doi.org/10.1021/ma102817z | *Macromolecules* 2011, 44, 2725–2734

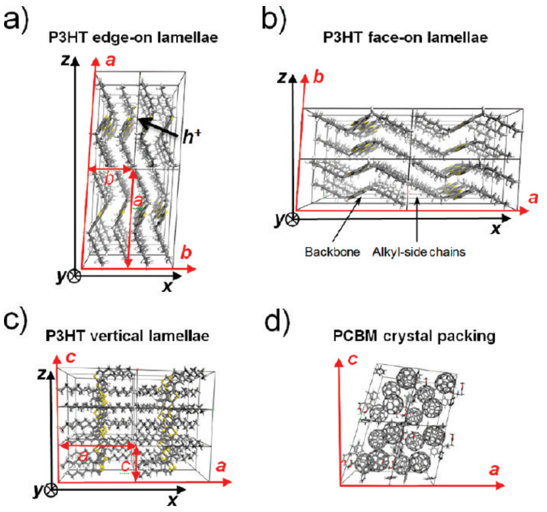

Figure 1. Illustration showing P3HT[3] and PCBM[12] crystal packing. The unit cells are enclosed by the boxes and are described by the lattice vectors *a*, *b*, and *c*. The P3HT alkyl- and π-stacking direction are along the *a* and *b* vectors, respectively. SiO_2 substrate coordinates are indicated with *x*, *y*, and *z*. Depending on the processing conditions, P3HT mainly self-organizes into (a) edge-on, (b) face-on, and (c) vertical lamellae (less likely).

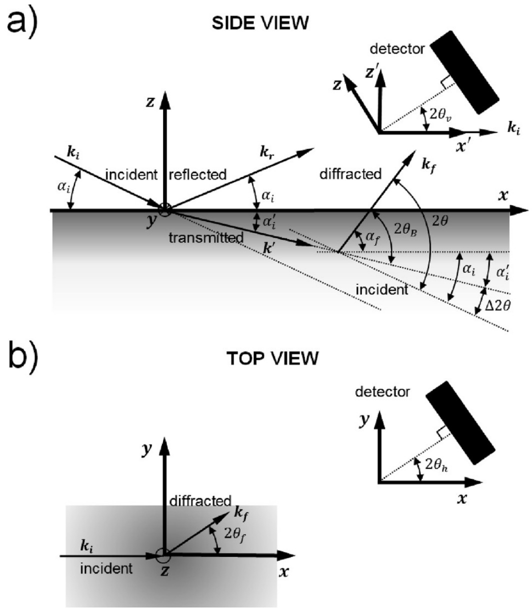

Figure 2. Illustration of the GI-WAXS diffraction geometry. The sample substrate reference system is *xyz*, whereas the diffractometer reference system is $x'yz'$.

substrate under usual processing conditions.[6a,13] As-spun PCBM films are usually made of small nanocrystallite aggregates, and annealing leads to the formation of large crystals.[9]

The as-spun blend of P3HT and PCBM has been described as a ternary system made of amorphous P3HT, crystalline P3HT, and PCBM aggregates.[14] A balance between P3HT−PCBM crystallinity (domain sizes maximized but not bigger than the exciton diffusion length[1b,9]) and phase separation (to maximize the interfacial area where excitons can be dissociated[9]) must be achieved to guarantee high power conversion efficiency (PCE).

Thermal annealing leads to a dramatic increase in the PCE with respect to as-spun devices.[15] Significant rearrangements in P3HT and PCBM crystalline domains occur during thermal annealing.[16] Grazing incidence X-ray diffraction (GI-XRD) has proved to be a powerful tool for investigating the nanomorphology of P3HT/PCBM BHJs with ex situ and in situ annealing.[4e,6a,7,9,13,14b,17] P3HT crystalline domain growth[9,14b] and PCBM interdiffusion[14b,18] within the amorphous P3HT are among the most relevant observed effects in literature.

In this work, the crystallographic changes inP3HT/PCBM blends, with different concentrations of P3HT, have been tracked during in situ thermal annealing by capturing synchrotron GI-XRD images over a period of 50 min, with a sampling time of ~7 s. The hot plate conditions, when annealing real OPVs, were reproduced with a temperature controller, simulating the temperature step experienced by the sample as the annealing commences. This study is complementary to that of Verploegen et al.,[9] who detailed structural changes on gradual heating of P3HT/PCBM blend films on silicon substrates. In contrast, we aim to follow the real-time kinetics during the first few minutes of the annealing, during which most of the efficiency gain in solar cells take place.[17k] In particular, we show that paracrystalline disorder occurs in P3HT/PCBM blends: we quantify the disorder and show that the spread of interplanar spacings narrows substantially during the first few minutes of the annealing, accompanied by a concomitant increase in angular misorientation of the P3HT lamellae. We also present a quantitative analysis of the effect of PCBM concentration on the crystallization rate of P3HT and show that PCBM has a plasticizing effect on crystallization of P3HT. Finally, using the incident angle dependence of the scattering, we show that the sample−air interface becomes rich in PCBM aggregates during the annealing.

■ EXPERIMENTAL SECTION

Sample Preparation. Thick (1 mm) SiO_2 wafers were cleaved into 1×1 cm^2 substrates, sonicated in acetone and isopropanol for 15 min each, rinsed with deionized water, and dried in a stream of nitrogen gas. Regioregular P3HT was purchased from Merck Chemicals (molecular weight 34.1 kg/mol, regioregularity 94.7%, polydispersity index 1.74), and PCBM was purchased from Solenne BV. Five P3HT/PCBM solutions (0, 33, 50, 67, 100 wt % P3HT) were prepared in a glovebox using chlorobenzene (30 mg/mL), stirred overnight, and spin-coated onto the SiO_2 substrates under ambient conditions. The average sample thickness was ~100 nm and the spin speed ~1600 rpm. GI-XRD measurements were perfomed at the I07 beamline (radiation energy 10 keV; direct beam aspect ratio ~1.732; monochromatic radiation resolution $<1 \times 10^{-4}$ KeV) (Diamond Light Source, U.K.). A home-built chamber was mounted onto a hexapod sample stage on the diffractometer. A goniometer, with a copper hot plate fixed to its top, was fastened at the center of the chamber. The sample was mounted onto the compact copper hot plate via a thermally conductive epoxy. Air scattering and background noise were reduced by filling the chamber with helium and remotely adjusting slits and a beamstop inside the chamber. Details of the chamber and the diffractometer can be found in the Supporting Information.

Grazing Incidence X-ray Diffraction. Figure 2 shows the grazing incidence wide-angle x-ray scattering (GI-WAXS) geometry used in this work.[19] The *z*-direction and the *xy* plane are perpendicular and parallel to the sample substrate, respectively. X-rays are incident on the sample with a wave vector $\boldsymbol{k}_i$ at a small angle α_i (out-of-plane (OOP) incident angle). The reflected beam, with wavevector $\boldsymbol{k}_r$, and the refracted/transmitted

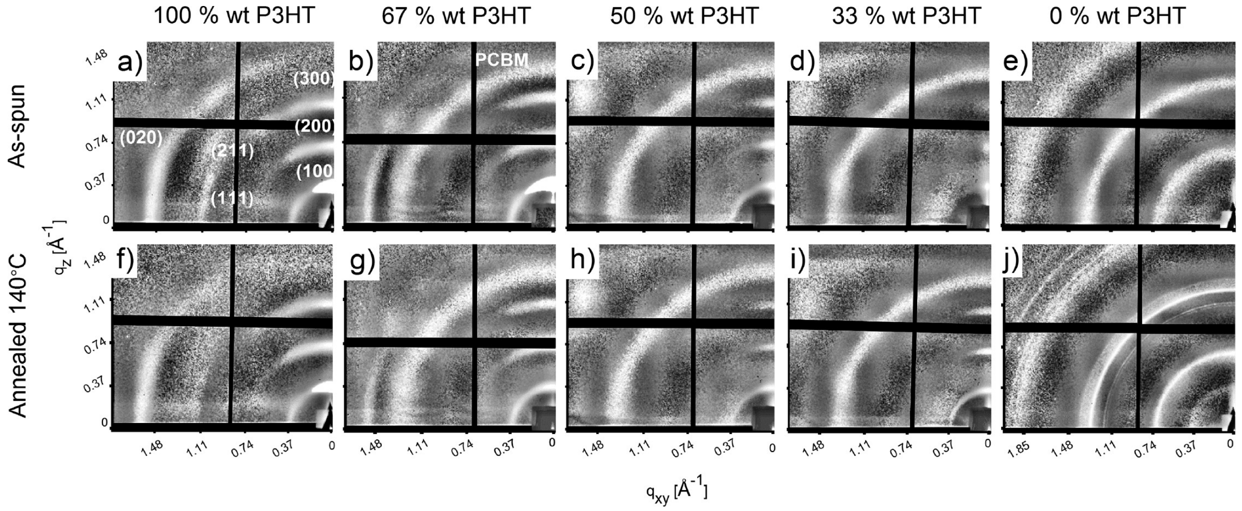

Figure 3. Diffraction patterns from blends of P3HT/PCBM before (30 °C) and after annealing (<34 °C) for samples with different concentrations of P3HT. Images contrast has been altered using adaptive local histogram normalization for illustration purposes only.

beam, with wavevector $\boldsymbol{k}'$, obey the Fresnel equations. The refracted beam travels at an angle of α_i' relative to the surface before being diffracted through the Bragg scattering angle $2\theta_B$.[19a] The diffracted beam emerges from the surface with a wavevector $\boldsymbol{k}_f$ at an angle 2θ from the incident beam. Whereas refraction effects are usually negligible for the diffracted beam, care needs to be taken to correct for refraction of the incident beam for $\alpha_i \approx \alpha_c$. The detector position is described with the horizontal and vertical angular coordinates $2\theta_h$ and $2\theta_v$, respectively. The in-plane (IP) exit angle is $2\theta_f$ and the out-of-plane exit angle is α_f.

A Pilatus 2 M (Dectris, Switzerland) area detector was used to collect images sequentially (5 s count time, ~2.4 s readout time) during in situ annealing. After an initial α_i scan and 20 images at 30 °C, the sample temperature was increased to 140 °C, within 30 s, using automatic temperature controller PID settings. The overshoot was 2.4 °C, and the temperature stabilized (to ±0.05 °C) at 140 °C after 20 s. After 39 min and 40 s, when 340 images had been collected, another α_i scan lasting 9 min and 45 s, was executed. In total, each sample was annealed for ~50 min. After annealing, the temperature controller was switched off, and the sample was cooled. The sample took 3 min and 45 s to drop below 34 °C, and, at this point, a further α_i scan was executed.

A detailed description of a computer program (GI-XRD-GUI), written for the analysis of the GI-XRD diffraction images, and the following derivations is reported in the Supporting Information. Detector pixel positions were related to diffraction angles by simple calibration procedures in which the direct beam position is monitored while scanning diffractometer angles. The scattering vector $\boldsymbol{q}$ can be related to the diffraction angles by the following relation

$$\boldsymbol{q} \overset{\text{def}}{=} \boldsymbol{k}_f - \boldsymbol{k}_i = k \begin{bmatrix} \cos\alpha_f \cos 2\theta_f \\ \cos\alpha_f \sin 2\theta_f \\ \sin\alpha_f \end{bmatrix} - k \begin{bmatrix} \cos\alpha_i \\ 0 \\ -\sin\alpha_i \end{bmatrix}$$

$$= k \begin{bmatrix} \cos\alpha_f \cos 2\theta_f - \cos\alpha_i \\ \cos\alpha_i \sin 2\theta_f \\ \sin\alpha_i + \sin\alpha_f \end{bmatrix} \qquad (1)$$

The resolution calculated in the range $|\boldsymbol{q}| \approx 0\ \text{Å}^{-1}$ and $|\boldsymbol{q}| \approx 1.87\ \text{Å}^{-1}$ was $(4.6 \pm 0.4) \times 10^{-3}\ \text{Å}^{-1}$. The scattering vector can be decomposed as $\boldsymbol{q}_\perp + \boldsymbol{q}_\parallel$, where $\boldsymbol{q}_\perp$ is the out-of-plane (OOP) component and $\boldsymbol{q}_\parallel$ is the IP component. Line profiles were extracted in pixels and then converted to $\boldsymbol{q}$ values using eq 1. IP line profiles $|\boldsymbol{q}_\parallel|$ (image azimuthal angle $\chi = 5°$, integration aperture $\Delta\chi = 10°$) and OOP line profiles $|\boldsymbol{q}_\perp|$ ($\chi = 90°$, $\Delta\chi = 10°$), were extracted for all scans. (See the illustration in Figure 4a,b). To compare IP with OOP line profiles, $q = |\boldsymbol{q}|$ is used as the abscissa. Tangential line profiles $I_\chi(\chi)$, with χ ranging from 0 to 90°, were extracted around Debye–Scherrer rings of interest (Figure 4c, inset). Integrated tangential line profiles were calculated as $I_{\text{int},\chi}(\zeta) = (\int_{\zeta}^{90°} I\chi(\zeta)\, d\zeta)/(\int_{0°}^{90°} I\chi(\zeta)\, dI\chi(\zeta))$, with $I_{\text{int},\chi}(\zeta) \in [0°, 90°]$, and rewritten as a function of χ as $I_{\text{int},\chi}(\chi)$.

A procedure for a batch adaptive background subtraction (via summation of several Gaussians) and peak detection was implemented in the GI-XRD-GUI program. Single peaks in the IP and OOP line profiles were fitted with an adaptive Pearson VII fitting procedure, involving an automatic step-by-step fitting, starting from the first peak up to the last one. Three significant parameters were extracted from each peak: full width half-maximum (FWHM), peak center, and peak integral.

■ RESULTS AND DISCUSSION

In the following sections, the qualitative evolution of diffraction patterns and the P3HT lamellar orientation for different P3HT concentrations is discussed. Refraction-corrected values for P3HT lattice constants along the alkyl-stacking direction are extracted and discussed. Peak widths (FWHM) are analyzed to separate the contribution from domain size and from disorder. Finally, a depth-resolved study on the concentration of PCBM is addressed.

Qualitative Evolution and P3HT Lamellar Orientation. Figure 3 shows the diffraction pattern images before and after annealing. Figure 4 shows the OOP line profiles and the IP line profiles. Five videos showing the evolution of peaks during in situ annealing of P3HT/PCBM films of different compositions can be found in the Supporting Information.

P3HT peaks have been indexed according to the model proposed by Kayunkid et al.[3] The combination of strong OOP (h00)-P3HT peaks and strong IP-(020)-P3HT peaks provides information about domain sizes, peak positions, and peak intensities along the direct lattice vectors $\boldsymbol{a}$ and $\boldsymbol{b}$, respectively, for the edge-on lamellae. In contrast, the combination of strong IP-(h00)-P3HT peaks and strong OOP-(020)-P3HT peaks provides the same information along direct lattice vectors $\boldsymbol{a}$ and $\boldsymbol{b}$ directions, respectively, for the

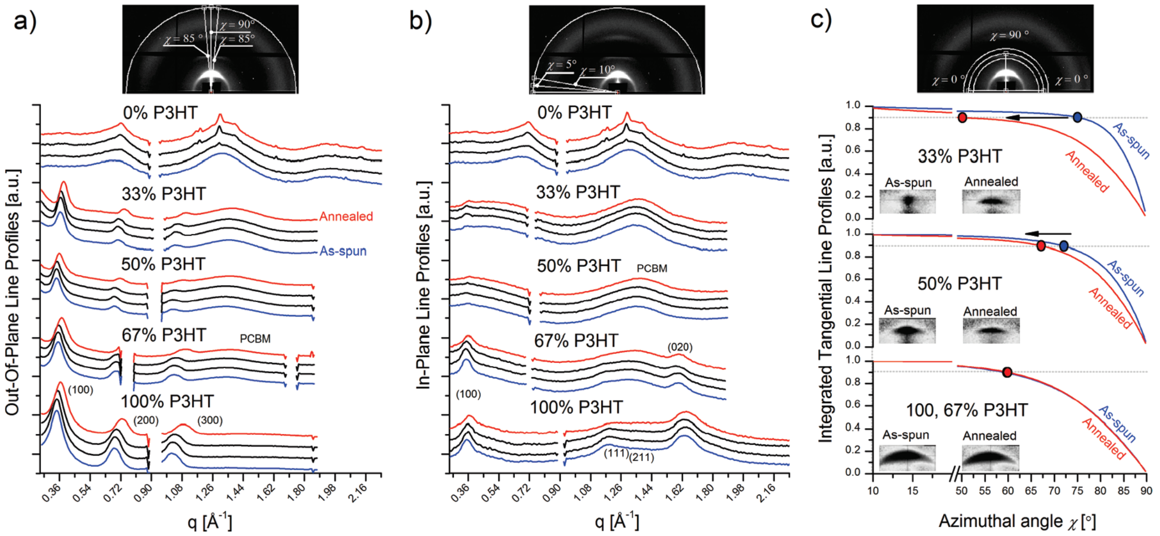

Figure 4. (a) Out-of-plane (OOP) and (b) in-plane (IP) line profiles before annealing (bottom blue line, as indicated for the OOP 33 wt % P3HT), in the early annealing stages (second line from the bottom), in the final annealing stages (third line), and after annealing (top red line) for P3HT/PCBM samples with different P3HT concentrations. This Figure has been built by stacking the logarithm of each line profiles and plotting the result as a linear plot in arbitrary units. (c) Integrated tangential line profiles and diffraction pattern details around the OOP-(200)-P3HT region, before and after annealing (c, insets). The three images on top of each graph show the convention used for the azimuthal angle and the integration slices used to extract OOP, IP, and tangential line profiles.

face-on lamellae. Integrated tangential line profiles $I_{\text{int},\chi,}(\chi)$ represent the probability of finding lamellae with $\angle(\boldsymbol{a}, xy)$ (angle between direct vector $\boldsymbol{a}$ and substrate plane xy) between χ and 90° as a function of χ. (Following a strict definition, $\angle(\boldsymbol{a}, xy)$ equal to 90 and 0° corresponds to the edge-on and face-on orientation, respectively. However, in the present discussion, we define in a wider sense: edge-on, the lamellae with $\angle(\boldsymbol{a}, xy)$ between 45 and 90°; face-on, the lamellae with $\angle(\boldsymbol{a}, xy)$ between 0 and 45°). It should be noticed that the OOP and IP P3HT sharp peaks arise from the crystalline P3HT. Weak reflections from the amorphous material can be observed in the IP line profiles as a broad peak around the IP-(100), onto which sharp crystalline P3HT peaks are superimposed.

For P3HT/PCBM blends, the only PCBM peak is a broad isotropic ring located at $q = 1.35$ Å^{-1}. For all concentrations containing P3HT, the OOP (h00)-P3HT peaks are clearly visible, with intensities increasing according to the increasing amount of P3HT. (h00)-P3HT higher order reflections are absent in the IP line profiles. As shown in the inset in Figure 4c, the OOP-(200) peak appears as an almost isotropic spot in the as-spun 33 wt % P3HT, becomes larger in the as-spun 50 wt % P3HT, and is tangentially broadened for the as-spun 67 wt % and pure P3HT. (A similar trend can be observed for the other two peaks (100) and (300), but for the (200) this is more evident in the images shown.) This shape change can be quantified with the (100) integrated tangential line profiles (Figure 4c). Note here that "x wt % P3HT" is used for the sake of brevity in place of "sample spin-coated from the solution containing x wt % of P3HT and $100 - x$ wt % of PCBM".

Sharp crystalline PCBM peaks cannot be observed in the as-spun blends, in agreement with other works.[4e,6a,13,14b,17c,17i] While annealing the 33 wt % P3HT, the OOP-(200) spot broadens tangentially, indicating a reduction in $\chi = \angle(\boldsymbol{a}, xy)$ due to tilting of the $\boldsymbol{a}$ axis, and narrows radially because of increasing domain size. Kim et al.[20] reported a study on the orientation of P3HT lamellae from P3HT/PCBM films ex situ GI-XRD and observed an analogous $\angle(\boldsymbol{a}, xy)$ spread after the annealing. Annealing levels out the differences in $\angle(\boldsymbol{a}, xy)$ between the samples with different concentrations, ending up with a situation in which most of the lamellae are edge-on oriented ($I_{\text{int},\chi,}(60°) \approx 90\%$), with an average angular spread between 60 and 90° for all samples. This corresponds to an angular spread of 5−65° between the normal of the π plane and the z axis, normal to the sample substrate (The angle between the $\boldsymbol{a}$ axis and the π plane is ~25° (indicated as θ_1 in Kayunkid et al.)).[3] This is probably beneficial for the vertical conduction (π hopping) within P3HT crystalline domains, as confirmed by previous reports, which show an increase in the conductivity of photoconductive AFM measurements[21] after annealing.

The (020)-P3HT ring is absent for the 33 and 50 wt % P3HT and appears only in the 67 wt % and pure P3HT. The (020)-P3HT ring is relatively highly oriented, and most of its intensity is concentrated in the IP direction ($\chi \approx 0°$). For this reason, the (020) peak appears in the OOP line profiles only as a weak shoulder (much weaker than the IP peak) as the P3HT concentration increases. The combination of a strong IP (100)-P3HT and weak OOP (020)-P3HT indicates that the remaining minority (<10%) of lamellae are face-on oriented.

Two other highly oriented peaks are visible in the as-spun pure P3HT. The first peak is at $q = 1.33$ Å^{-1}, whereas the second is at $q = 1.93$ Å^{-1}, and most of their intensity is concentrated at $\chi \approx 10$ and 30°, respectively. These peaks have been identified as the (111) and (211) reflections, respectively. The presence of PCBM interferes with the formation of these two peaks. The same peaks have been observed in diffraction patterns on P3HT nanowires, although sharper and more intense. (See Figure S10 in the Supporting Information and ref 22.)

During the annealing, pure PCBM exhibits an evolution in the diffraction pattern that strongly differs from the blends (Figures 3 and 4). Three isotropic rings are observed in as-spun PCBM. The first, at $q = 0.71$ Å^{-1}, becomes gradually sharper during annealing. The second, at $q = 1.35$ Å^{-1}, is the one observed in the blend. A sharp peak ($q = 1.30$ Å^{-1}) close to the second ring continuously

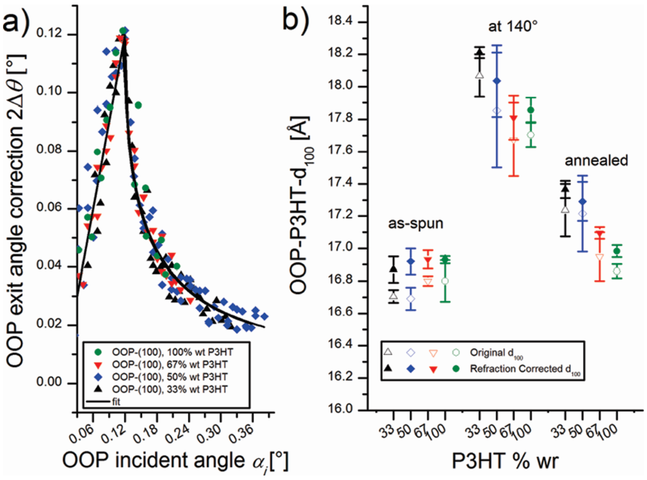

Figure 5. (a) Correction term $2\Delta\theta = \alpha_f - \alpha_{fB}$ that must be applied when determining the OOP-d_{100} from the measured OOP exit angle α_f. The graph was built in the same manner described by Toney et al.[19a] The average Pearson correlation coefficient calculated for the fits was $R^2 = 0.9970$.[25] (b) Effect of refraction correction on OOP-d_{100}. ("At 140 °C" refers to the final stage of the annealing.)

grows in intensity throughout the annealing process. Other sharp rings appear at q = 1.15, 1.18, and 1.39 Å^{-1}. Finally, annealing provokes the growth of several sharp peaks evolving from a third broad peak at q = 2.00 Å^{-1}. The peaks in the as-spun and annealed line profiles are due to the superposition of a large number of reflections from several Miller planes and could not be unequivocally indexed. Highly oriented PCBM crystallites, as reported in Verploegen et el.,[9] have not been observed, most likely because of differences in sample preparation. (Main differences: solvent, substrate treatment, spin speed and sample thickness. Solvent: we used chlorobenzene (boiling point (bp) 131.7 °C, polarity index (P') 2.7); they used chloroform (bp 61.2 °C, P' = 4.8). Substrate treatment: they used oxygen plasma etch. Spin speed: we used ~1600 rpm (60 s), they used 400 rpm (10 s) and 1000 (60 s). Sample thickness: we had ~100 nm; they had ~20 nm. Substrate treatment: they used oxygen plasma etch.)

Unit Cell Dynamics During Annealing. OOP d spacings measured at low q values can be affected by refraction effects, particularly when the incident angle α_i is close to its critical value α_c.[19a,23] The α_i scans can be used to improve the accuracy of the OOP-(100)-P3HT d spacing (OOP-$d_{100} = 2\pi/q$), which corresponds to the P3HT lattice constant in the $\boldsymbol{a}$ direction, measured during the annealing scans. The OOP-d_{100} versus α_i shows a nonconstant profile with a minimum at $\alpha_i = \alpha_c$ because of refraction effects (examples of curves shown in Supporting Information, Figure S11). An expression for the correction term $2\Delta\theta$ required to account for refraction of the transmitted beam, prior to diffraction can be derived. Theoretical details are reported in the Supporting Information. Describing the sample as a uniform dielectric with a complex refractive index $n = 1 - \delta - j\beta$,[19a] we can write the measured OOP exit angle as[19a,23]

$$\begin{aligned}\alpha_f &= 2\Delta\theta + \alpha_{fB}\\ &= \alpha_i + \alpha_{fB} - \frac{1}{\sqrt{2}}\sqrt{\sqrt{(\alpha_i{}^2 - \alpha_c{}^2)^2 + 4\beta^2} + (\alpha_i{}^2 - \alpha_c{}^2)}\end{aligned} \tag{2}$$

Table 1. P3HT Thermal Expansion Coefficients along the *a* Direction during Heating and Cooling, Respectively[a]

wt % P3HT	$\alpha_T \times 10^{-4}$ [K^{-1}] 33	50	67	100
heating	5.23	5.28	6.17	7.25
cooling	3.95	3.31	3.37	3.91

[a] Average standard deviation is $\bar{\sigma} \approx 0.02$ Å. During heating, both expansion and crystallization occur, whereas only contraction occurs on cooling.

where $a_c = (2\delta)^{1/2}$ and α_{fB} is the correct OOP exit angle, as indicated in Figure 2. To extract α_{fB}, values of α_f, obtained by scanning α_i through the critical angle, can be fitted using eq 2 with α_{fB}, α_c, and β as fitted parameters. All fitting curves are almost overlapped. The average extracted critical angle is $\alpha_c \approx 0.12°$, from which $\delta = (3.10 \pm 0.03) \times 10^{-6}$ is estimated, whereas the imaginary part of the refractive index is $\beta = (2.0 \pm 0.5) \times 10^{-9}$. The maximum error committed on the Bragg angle is $2\Delta\theta \approx 0.12°$ at $\alpha_i = \alpha_c$. The resulting correction term, shown in Figure 5, can be used to apply a small correction to the OOP-d_{100} (The in-plane exit angle $2\theta_f$ is zero in the OOP line profiles)

$$d_{100} = \frac{2\pi}{|q_\perp|'} = \frac{\sqrt{2}\pi}{k\sqrt{1 - \cos(\alpha_i + \alpha_{fB})}} \tag{3}$$

This refraction correction is insignificant for the (020)-P3HT and PCBM d spacing and for the FWHM values.

Figure 5b shows the OOP-d_{100} before and after the refraction correction. OOP-d_{100} is subject to thermal expansion; that is, the (100)-P3HT peak shifts to lower q values during annealing. During annealing a continuous reduction in the OOP-d_{100} is observed (Figure S13, Supporting Information). After cooling, after the end of the annealing, the d_{100} assumes higher values than the as-spun d_{100}, the difference being more pronounced with increasing amounts of PCBM. This irreversible lattice expansion has been observed in other studies on pure P3HT[7,9,24] and P3HT/PCBM blends[9] and seems to be independent of the annealing strategy and duration. The apparent thermal expansion coefficients[7] deduced from the heating ramp ranges from $\alpha_T \approx 7.25 \times 10^{-4}$ K^{-1} (33 wt % P3HT) to $\alpha_T \approx 5.23 \times 10^{-4}$ K^{-1} (100 wt % P3HT), whereas the corresponding coefficients deduced from the cooling ramp at the end of the annealing are less dependent on composition, with an average value of $\alpha_T \approx (3.6 \pm 0.3) \times 10^{-4}$ K^{-1}. It should be noticed that the evolution of OOP-d_{100} and corresponding expansion coefficient on heating are also influenced by the crystallization process. The thermal expansion coefficient variation is summarized in Table 1. Verploegen et al.,[9] in line with our results, observed increasing P3HT expansion coefficients along the $\boldsymbol{a}$ direction in the heating ramp with increasing P3HT concentrations.

Figure S13 (Supporting Information) shows the average IP-d_{020} corresponding to half of the lattice constant in the $\boldsymbol{b}$ direction. A comparison between the values extracted for all blends did not reveal any significant differences. The behavior of the IP-d_{020} was completely reversible, ranging from ~3.87 Å at room temperature to ~3.89 Å at 140 °C ($\alpha_T \approx (4.3 \pm 0.4) \times 10^{-5}$ K^{-1}). The thermal expansion behavior for P3HT is highly anisotropic, being an order of magnitude higher in the $\boldsymbol{a}$ direction than in the $\boldsymbol{b}$ direction. The anisotropy is greatest for pure P3HT and hence appears to be intrinsic to P3HT rather than being induced by the presence of PCBM. The physical cause of the anisotropic thermal expansion cannot be unambiguously determined from diffraction results.[24] Tashiro et al.[11a] showed that the large expansion along the ***a*** direction upon heating is accompanied by a weakening of vibrational lines associated with the all-trans conformation of the alkyl side chains and a concomitant strengthening of those associated with gauche conformations, leading them to conclude that this expansion is largely driven by vibrational interactions between side chains,[11] but this evidence is insufficient to establish a causal link.

Figure S13 (Supporting Information) shows also the average PCBM *d* spacing. A comparison between the values extracted for all blends did not reveal any significant differences. The average behavior for the d_{PCBM} is reversible, ranging from ~4.64 Å at room temperature to ~4.71 Å at 140 °C ($\alpha_T \approx (1.23 \pm 0.03) \times 10^{-4}\ \mathrm{K}^{-1}$).

Crystallization Dynamics During Annealing. OOP-(h00)-P3HT domain sizes (domain size is synonymous of coherence length of the single crystalline domain (i.e., lamella) along the specified direction) (OOP-L_{h00}) versus annealing time give insight into the ongoing crystallization of the majority of the edge-on lamellae along the ***a*** direction. (Because in OOP line profiles construction $\chi = 90°$ and $\Delta\chi = 10°$, OOP (h00)-P3HT peaks provide information about the domain size of lamellae with $\angle(\boldsymbol{a}, xy)$ between 85 and 90°.) On the other side, IP-(020)-P3HT domain sizes (IP-L_{020}) allow the study of the growth of the same lamellae along the ***b*** direction. (Because in the IP line profiles construction $\chi = 5°$ and $\Delta\chi = 10°$, IP-(020)-P3HT peaks provide information about the domain size of lamellae with $\angle(\boldsymbol{b}, xy)$ between 0 and 10°.) OOP-(h00) FWHM (OOP-Δq_{h00}) was available for $h = 1$, 2, and 3. If the Δq_{h00} are the same for $h = 1$, 2, and 3, then the FWHMs are dominated by crystallite size.[5b] This model is represented by the Scherrer's equation,[26] which gives an approximation of the domain sizes. However, Δq_{h00} calculated for different h, within the same line profile, increased with h. The increase in FWHM with the order can be attributed to variation in the interplanar spacing between adjacent grains.[5b] This indicates that Δq_{h00} cannot be interpreted with the simple Scherrer's equation, and a paracrystalline correction should be applied to obtain the correct domain sizes.[27] The paracrystalline theory[27] for which an approximate function can be employed[26] allows for the separation of the disorder contribution from the real domain sizes. (Details are provided in the Supporting Information.) Here by using a 1D paracrystal model we characterize the paracrystalline disorder within the crystalline domains caused by a Gaussian spread in the backbone spacings along the ***a*** direction. The measured Δq_{h00} can be written as[26] $\Delta q_{h00}^2 = \Delta q_c^2 + \Delta q_{b,h00}^2$, where Δq_c and $\Delta q_{b,h00}$ are the contributions to the finite crystallite size and distortions (paracrystallinity), respectively.[26] The crystallite sizes along the ***a*** direction are given by Scherrer's equation[26] $L_{\boldsymbol{a}} \approx 0.9 \times 2\pi/\Delta q_c$, whereas $\Delta q_{b,h00}$ can be approximated as $\pi^2 g_{h00}^2\, h^2/d_{h00}$, where g_{h00} is proportional to the degree of disorder in the crystal. The measured Δq_{h00}^2 can be written as $\boldsymbol{y} = y_0 + m\boldsymbol{x}$ with

$$\begin{cases} \boldsymbol{y} = \dfrac{[\Delta q_{100}^2 \quad \Delta q_{200}^2 \quad \Delta q_{300}^2]}{(2\pi)^2} \\ y_0 = \dfrac{\Delta q_c^2}{(2\pi)^2} = \dfrac{1}{L_a^2} \\ m = \dfrac{(\pi g_{h00})^4}{\mathrm{d}_{h00}^2} \text{ for } h = 1, 2, 3 \\ \boldsymbol{x} = [1 \quad 2 \quad 3]^4 \end{cases} \tag{4}$$

Fitting the line $\boldsymbol{y}$ versus $\boldsymbol{x}$, y_0 and m can be extracted for all measurements.[26] The domain sizes are extracted from $L_{\boldsymbol{a}} = (0.9/y_0)^{1/2}$, whereas the g factors are extracted from $g_{h00} = (m d_{h00}^2/\pi)^{1/4}$. d_{h00} and Δq_{h00} were available for the four composition ratios as a function of annealing time. Figure 6a shows the domain sizes obtained using Scherrer's equation on the measured

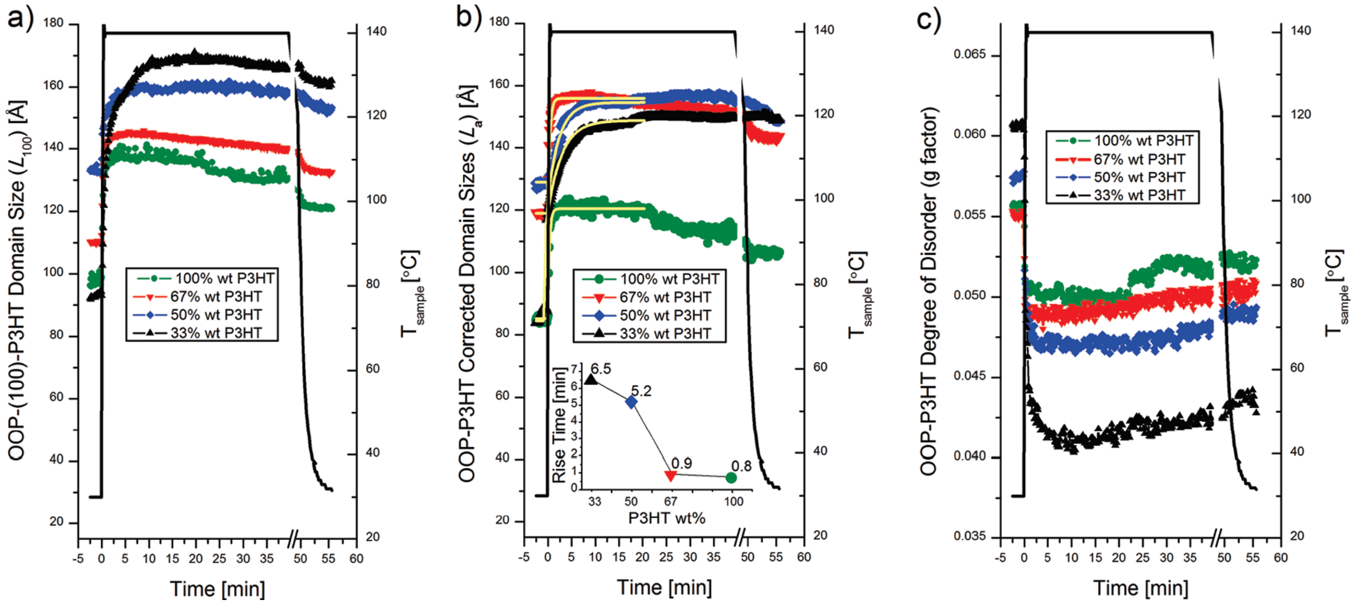

Figure 6. (a) OOP-(100)-P3HT domain sizes (L_{100}) calculated using the Scherrer's equation on the original FWHM. (b) OOP-P3HT domain sizes (L_a) calculated using the paracrystallinity correction and transitory fit (yellow lines). Rise times as a function of the P3HT concentration (b, inset). (c) OOP-P3HT degree of disorder. (The g factor is a dimensionless quantity.) The average standard deviation (between samples with the same wt % P3HT) of each curve was $\bar{\sigma} \approx 1.5$ Å for the domain sizes, and ~1×10^{-3} for the g factor. The average Pearson correlation coefficient for the step responses fits was $R^2 = 0.9956$.

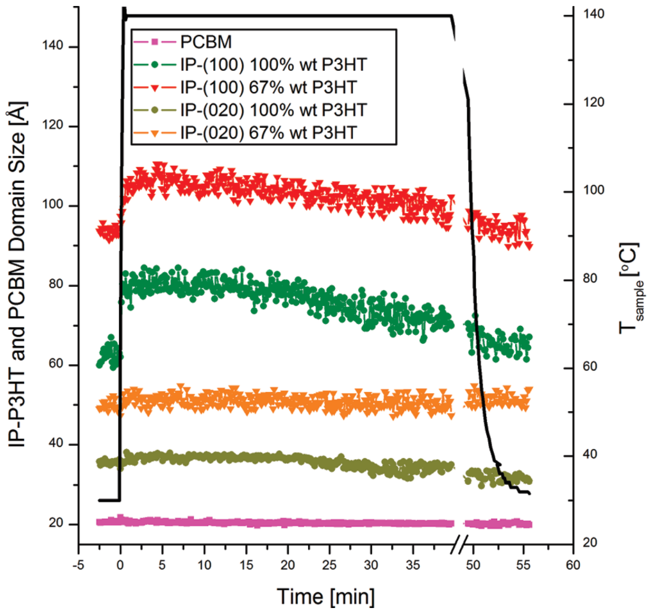

Figure 7. IP-(020)-P3HT (≈ 3.2 Å), IP-(100)-P3HT (≈ 5.2 Å), and average (≈ 0.6 Å) PCBM coherence lengths calculated with Scherrer's equation.

Δq_{h00}. The values observed for pure P3HT are consistent with the ones reported by Joshi et al.[7] (~95 Å as-spun, 137 Å at 140 °C). Increases in the domain sizes along the P3HT ***a*** direction in pure P3HT and in the blend have been reported in several works.[6b,9,17b,17e,20,28]

Examples of the curve fitting (33 wt %) obtained from the plot of ***y*** versus ***x*** for all 390 points of the annealing curve are shown in the Supporting Information (Figure S13). Because the three calculated $\boldsymbol{g}_{h00}$ vectors (for all the three orders) are almost overlapped ($\bar{\sigma} \approx 1.3 \times 10^{-4}$), only the average has been displayed. Figure 6b shows the L_a calculated using the paracrystalline correction. (The paracrystalline correction was not possible on the IP-L_{0k0}, IP-L_{h00}, and L_{PCBM} because just one order of peak was available.) The effect of the correction produces similar values for L_a in all blends, which can be quantified in terms of the average standard deviation, varying from ~13 to ~5 Å, between the old and the corrected values. The crystallization dynamics, in the first minutes, can be described using a first-order linear time invariant model[29] responding to an annealing step

$$L_a(t) = \begin{cases} p\cdot\left(1 - e^{-(t-t_0)/T}\right) + L_a(t_0) & \text{for } t > t_0 \\ L_a(t_0) & \text{for } t < t_0 \end{cases} \qquad (5)$$

where T is the time constant, p is the asymptotic amplitude value representing the average domain size during the annealing, $L_a(t_0)$ is the domain sizes for the as-spun sample, and t_0 is the moment at which the heating step begins. The calculated rise times ($t_r \approx T \times 2.2$)[29] are strongly correlated with the concentration of P3HT (Figure 6b, inset), ranging from ~6.5 min for the 33 wt % to ~0.8 min for pure P3HT. Finally, Figure 6c represents the degree of paracrystalline disorder. For all samples, the g factor abruptly decreases in the first minute of annealing, showing the lowest degree of disorder for the 33 wt % P3HT. Therefore, annealing leads to healing of stacking defects along the ***a*** direction (Supporting Information, video S6). The discussed dynamics suggest that PCBM behaves like a plasticizer[30] for P3HT. The PCBM plasticizing effect is confirmed by the decrease in the melting peak temperature (T_m)[31] for decreasing concentration of P3HT, as reported by Müller et al.[16b] in differential scanning calorimetry (DSC) thermograms recorded during heating. When the sample has cooled down, an average variation (between the last values measured at 140 °C and the last values measured at <35 °C) of −4% in L_a is observed for all samples. This variation corresponds to the one observed in d_{100} and thus can be attributed to a thermal contraction of the crystalline domains along the ***a*** direction. Similar L_a final values are reached for all blends (<100 wt % P3HT), whereas pure P3HT shows lower values. The result that the L_a values after annealing are similar for all three blend concentrations and larger than the corresponding value for pure P3HT is consistent with the reduced crystallization rate, characterized by the increased rise times noted above, observed with increased PCBM concentration. A reduced crystallization rate provides time for molecules to attain their lowest energy sites, thus increasing the observed domain size. This is a similar effect to the use of high boiling-point solvents such as trichlorobenzene, in which reduced rates of evaporation lead to reduced crystallization rates and higher crystallinity.[17j] In agreement with Treat et al.,[14b] we exclude the possibility that PCBM intercalates between P3HT chains (within crystalline domains), and we support the idea that during annealing PCBM diffuses into the amorphous P3HT regions. Growth of the P3HT crystalline domains, with concomitant exclusion of PCBM, improves OPV performance, although excessive growth beyond the exciton diffusion length will limit exciton dissociation and hence degrade performance.[9,14b] It should be noted that the relative domain sizes for pure P3HT and the blends should not be directly interpreted as measures of film crystallinity. As seen in Figure 4a, the OOP-(100) peak intensity decreases strongly on PCBM addition, indicating that the volume of crystalline material in the pure P3HT film is the highest.

Conversely IP-L_{020} (Figure 7) did not show any relevant growth. It can be concluded that the edge-on lamellae grow along the ***a*** direction only, with dynamics that depend on the concentration of P3HT. It is likely that the local PCBM concentration along the edges of the lamellae, at the interface with amorphous P3HT, strongly influences the kinetics of domain growth along the ***a*** direction. The crystallographic ***b*** axis lies along the π-stacking direction along the length of the P3HT crystalline lamellae. The lack of domain growth in this direction implies that annealing does not improve order in the π-stacking between P3HT molecules.

The variation of the IP-L_{100} with annealing time gives insight into the ongoing crystallization of the minority of the face-on lamellae along the ***a*** direction. OOP-L_{020} would allow for the exploration of the growth of the face-on domain sizes along the ***b*** direction, but unfortunately this information is not available. The IP-L_{100} peak signal-to-noise ratio (SNR) is too low for the samples with a P3HT concentration ≤50 wt % to allow proper fitting. Figure 7 shows the IP-L_{100} variation for the 30 wt % and the pure P3HT. The IP-L_{100} reaches a peak in the first phase of annealing (~3 min) and after that reduces, smoothly and continuously, back to the initial value after cooling.

The sharp peak around $q = 1.30$ Å^{-1} was deconvolved with respect to the broad peak at $q = 1.35$ Å^{-1}, in the pure PCBM. After an initial growth, the sharp peak stabilized with an FWHM of ~0.021 Å^{-1}, corresponding to an approximate domain size of ~27 nm.

The amorphous L_{PCBM} calculated for the blends showed the same trend and similar values. The average L_{PCBM} values are plotted

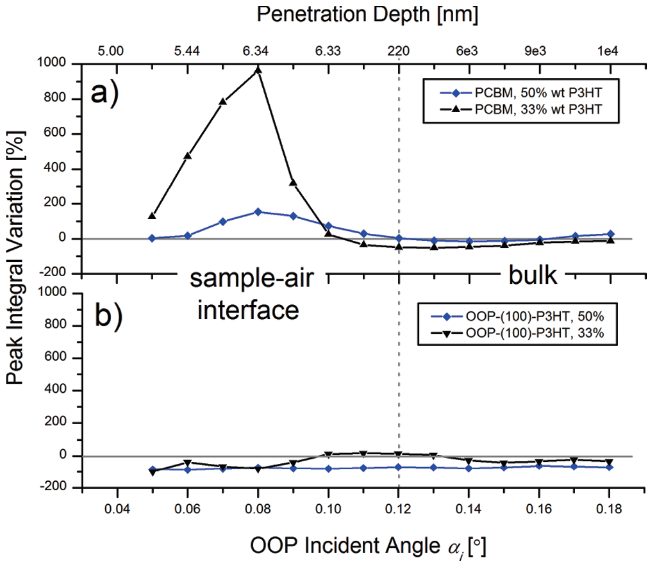

Figure 8. (a) PCBM peak integral percentage variation and (b) P3HT peak integral percentage variation between as-spun and annealed samples for different P3HT concentrations.

in Figure 7 and, in agreement with other GI-XRD reports,[13,17a,17c] do not show significant changes during annealing. Because the phase segregation occurring during annealing is primarily driven by P3HT crystallization, the resulting aggregation of PCBM molecules does not necessarily lead to the formation of nanocrystals.

Depth-Resolved PCBM Concentration. The integral of the fitted peaks is directly proportional to the amount of crystalline material. Figure 8 shows the percentage variation between the as-spun and the annealed films of the (100)-P3HT peak integral versus α_i. Because k' is complex along the z direction, the X-rays are attenuated along the z direction, sampling a volume defined by the penetration depth[32]

$$\Lambda \stackrel{\text{def}}{=} \frac{1}{2k\,\mathrm{Im}(\alpha_i')} \approx \left[\sqrt{2}k\sqrt{\sqrt{(\alpha_i^2-\alpha_c^2)^2+(-2\beta)^2}-(\alpha_i^2-\alpha_c^2)}\right]^{-1} \tag{6}$$

The calculation of β and α_c, previously described earlier, allows for the calculation of the penetration depth and for the establishment of a correspondence between α_i and Λ. Below the critical angle, the X-rays undergo total external reflection. An evanescent wave propagates along the sample−air interface and its amplitude decays exponentially with depth into the film (penetration depth ∼6 nm). The secondary x axis in Figure 8 displays the penetration depth as a function of α_i. The relative intensity after annealing can be compared for the sample−air interface and the bulk of the film. Annealing causes an increase in the PCBM relative intensity at the film surface, which is proportional to the amount of PCBM in the 33 and 50 wt % P3HT. This gradient could indicate an increase in the concentration of PCBM aggregates at the sample−air interface for the 33 and the 50 wt % P3HT. Kiel et al.[18] reported neutron reflectivity results showing that in the as-spun blend there is increased PCBM concentration at both the bulk of the film and at the sample−air interface. Upon annealing they found an increase in the PCBM concentration at the sample−air interface, which they associate with PCBM excluded from crystallizing P3HT but little change at the buried interface with the substrate. In another work, small-angle neutron scattering results showed aggregates of PCBM at the sample−air interface of annealing.[33] The authors observed an increase in PCBM concentration at the sample−air interface on annealing, which is consistent with that shown in Figure 8. Their small-angle scattering and our wide-angle scattering results together point to aggregation of small PCBM particles (of 1−3 nm dimension) at the film−air interface rather than the growth of extended PCBM crystals for films spun from chlorobenzene and annealed at 140 °C. Our results are also consistent with ellipsometry data showing that upon annealing PCBM molecules diffuse to the surface where they can either aggregate or crystallize.[34]

CONCLUSIONS

Detailed analysis of time-resolved GI-XRD results is used to quantify the structural changes occurring inP3HT/PCBM films during thermal annealing at 140 °C in terms of P3HT lamellar orientation spread, backbones spacing along the alkyl-stacking direction, domain sizes, paracrystalline disorder, and the relative distribution of PCBM aggregates between bulk and sample−air interface. Our as-spun films are mainly edge-on oriented, with a minority of face-on lamellae. Strongly anisotropic thermal expansion is observed during initial heating with the coefficient of thermal expansion along the alkyl-staking direction in P3HT being approximately a factor of 10 greater than along the π-stacking direction and a factor of 5 greater than PCBM. During the first 3−5 min of the annealing, the P3HT domain size along the alkyl-stacking direction increases rapidly with a composition-dependent time constant. This is accompanied by a decrease in the paracrystalline spread in d spacing along this direction and with a broadening of the angular orientational spread. The PCBM amorphous ring is largely unaffected by annealing: no large PCBM crystallites were observed, except for pure PCBM. The crystallization dynamics suggest that PCBM acts as a plasticizer for P3HT. For samples with high PCBM content (50 and 33 wt % P3HT), analysis of the peak integrals as a function of the incident angle, shows a dramatic increase in the concentration of PCBM aggregates close to the sample−air interface.

ASSOCIATED CONTENT

Ⓢ Supporting Information. Experimental details; data analysis (calibration equations, sample−detector distance, conversion pixels q values, out-of-plane line profiles, remarks on P_{0x}, P_{0y} accuracy, line profiles extraction, line profiles fitting); refraction correction; paracrystalline disorder; results (P3HT nanowires, d spacing vs α_i, d spacings vs time and annealing temperature); five videos showing 390 images from in situ annealing of P3HT/PCBM films of different compositions; and a video showing the flattening of $\Delta q_{h00}^2/(2\pi)^2$ versus n^4 due to the annealing. This material is available free of charge via the Internet at http://pubs.acs.org.

AUTHOR INFORMATION

Corresponding Author

*E-mail: samuele.lilliu@hotmail.it. Tel: +44 (0)29 2087 0162 (lab). Fax: +44 (0)29 2087 4056.

ACKNOWLEDGMENT

We thank the I07 team for help at the beamline. We would like to thank R. Tucker for help with the instrumentation.

This work was partially funded by the Engineering and Physical Sciences Research Council (EPSRC) grant number EP/F016255, EP/F023200, EP/G031088, EP/F061757, EP/F056710, and Research Councils U.K. (RCUK). We acknowledge the Royal Society as well.

■ REFERENCES

(1) (a) Sariciftci, N. S.; Smilowitz, L.; Heeger, A. J.; Wudl, F. Photoinduced Electron Transfer from a Conducting Polymer to Buckminsterfullerene. *Science* **1992**, *258*, 1474. (b) Carsten, D.; Vladimir, D. Polymer−Fullerene Bulk Heterojunction Solar Cells. *Rep. Prog. Phys.* **2010**, *73*, 096401. (c) Thompson, B. C.; Fréchet, J. M. J. Polymer-Fullerene Composite Solar Cells. *Angew. Chem., Int. Ed.* **2008**, *47*, 58.

(2) (a) Park, S. H.; Roy, A.; Beaupre, S.; Cho, S.; Coates, N.; Moon, J. S.; Moses, D.; Leclerc, M.; Lee, K.; Heeger, A. J. Bulk Heterojunction Solar Cells with Internal Quantum Efficiency Approaching 100%. *Nat. Photon.* **2009**, *3*, 297–302. (b) Green, M. A.; Emery, K.; Hishikawa, Y.; Warta, W. Solar cell efficiency tables (Version 35). *Prog. Photovoltaics* **2010**, *18*, 144.

(3) Kayunkid, N.; Uttiya, S.; Brinkmann, M. Structural Model of Regioregular Poly(3-hexylthiophene) Obtained by Electron Diffraction Analysis. *Macromolecules* **2010**, *43*, 4961–4967.

(4) (a) Kline, R. J.; DeLongchamp, D. M.; Fischer, D. A.; Lin, E. K.; Richter, L. J.; Chabinyc, M. L.; Toney, M. F.; Heeney, M.; McCulloch, I. Critical Role of Side-Chain Attachment Density on the Order and Device Performance of Polythiophenes. *Macromolecules* **2007**, *40*, 7960–7965. (b) Sirringhaus, H.; Brown, P. J.; Friend, R. H.; Nielsen, M. M.; Bechgaard, K.; Langeveld-Voss, B. M. W.; Spiering, A. J. H.; Janssen, R. A. J.; Meijer, E. W.; Herwig, P.; de Leeuw, D. M. Two-Dimensional Charge Transport in Self-Organized, High-Mobility Conjugated Polymers. *Nature* **1999**, *401*, 685–688. (c) Zen, A.; Saphiannikova, M.; Neher, D.; Grenzer, J. r.; Grigorian, S.; Pietsch, U.; Asawapirom, U.; Janietz, S.; Scherf, U.; Lieberwirth, I.; Wegner, G. Effect of Molecular Weight on the Structure and Crystallinity of Poly(3-hexylthiophene). *Macromolecules* **2006**, *39*, 2162–2171. (d) Ma, W.; Yang, C.; Gong, X.; Lee, K.; Heeger, A. J. Thermally Stable, Efficient Polymer Solar Cells with Nanoscale Control of the Interpenetrating Network Morphology. *Adv. Funct. Mater.* **2005**, *15*, 1617–1622. (e) Erb, T.; Zhokhavets, U.; Gobsch, G.; Raleva, S.; Stühn, B.; Schilinsky, P.; Waldauf, C.; Brabec, C. J. Correlation Between Structural and Optical Properties of Composite Polymer/Fullerene Films for Organic Solar Cells. *Adv. Funct. Mater.* **2005**, *15*, 1193–1196. (f) Aryal, M.; Trivedi, K.; Hu, W. Nano-Confinement Induced Chain Alignment in Ordered P3HT Nanostructures Defined by Nanoimprint Lithography. *ACS Nano* **2009**, *3*, 3085–3090.

(5) (a) Joshi, S.; Grigorian, S.; Pietsch, U. X-ray Structural and Crystallinity Studies of Low and High Molecular Weight Poly (3-hexylthiophene). *Phys. Status Solidi A* **2008**, *205*, 488–496. (b) Salleo, A.; Kline, R. J.; DeLongchamp, D. M.; Chabinyc, M. L. Microstructural Characterization and Charge Transport in Thin Films of Conjugated Polymers. *Adv. Mater.* **2010**, *22*, 3812–3838. (c) DeLongchamp, D. M.; Vogel, B. M.; Jung, Y.; Gurau, M. C.; Richter, C. A.; Kirillov, O. A.; Obrzut, J.; Fischer, D. A.; Sambasivan, S.; Richter, L. J.; Lin, E. K. Variations in Semiconducting Polymer Microstructure and Hole Mobility with Spin-Coating Speed. *Chem. Mater.* **2005**, *17*, 5610–5612.

(6) (a) Chen, H.-Y.; Yang, H.; Yang, G.; Sista, S.; Zadoyan, R.; Li, G.; Yang, Y. Fast-Grown Interpenetrating Network in Poly-(3-hexylthiophene): Methanofullerenes Solar Cells Processed with Additive. *J. Phys. Chem. C* **2009**, *113*, 7946–7953. (b) Kline, R. J.; McGehee, M. D.; Kadnikova, E. N.; Liu, J.; Fréchet, J. M. J.; Toney, M. F. Dependence of Regioregular Poly(3-hexylthiophene) Film Morphology and Field-Effect Mobility on Molecular Weight. *Macromolecules* **2005**, *38*, 3312–3319.

(7) Joshi, S.; Pingel, P.; Grigorian, S.; Panzner, T.; Pietsch, U.; Neher, D.; Forster, M.; Scherf, U. Bimodal Temperature Behavior of Structure and Mobility in High Molecular Weight P3HT Thin Films. *Macromolecules* **2009**, *42*, 4651–4660.

(8) (a) Salleo, A. Charge Transport in Polymeric Transistors. *Mater. Today* **2007**, *10*, 38–45. (b) Liu, C.; Oshima, K.; Shimomura, M.; Miyauchi, S. Anisotropic Conductivity-Temperature Characteristic of Solution-Cast Poly(3-hexylthiophene) Films. *Synth. Met.* **2006**, *156*, 1362–1367.

(9) Verploegen, E.; Mondal, R.; Bettinger, C. J.; Sok, S.; Toney, M. F.; Bao, Z. Effects of Thermal Annealing Upon the Morphology of Polymer−Fullerene Blends. *Adv. Funct. Mater.* **2010**, *20*, 3519–3529.

(10) Brinkmann, M.; Rannou, P. Molecular Weight Dependence of Chain Packing and Semicrystalline Structure in Oriented Films of Regioregular Poly(3-hexylthiophene) Revealed by High-Resolution Transmission Electron Microscopy. *Macromolecules* **2009**, *42*, 1125–1130.

(11) (a) Tashiro, K.; Ono, K.; Minagawa, Y.; Kobayashi, M.; Kawai, T.; Yoshino, K. Structure and Thermochromic Solid-State Phase Transition of Poly(3-alkylthiophene). *J. Polym. Sci., Part B: Polym. Phys.s* **1991**, *29*, 1223–1233. (b) Pascui, O. F.; Lohwasser, R.; Sommer, M.; Thelakkat, M.; Thurn-Albrecht, T.; Saalwächter, K. High Crystallinity and Nature of Crystal-Crystal Phase Transformations in Regioregular Poly(3-hexylthiophene). *Macromolecules* **2010**, *43*, 9401–9410.

(12) Rispens, M. T.; Meetsma, A.; Rittberger, R.; Brabec, C. J.; Sariciftci, N. S.; Hummelen, J. C. Influence of the solvent on the crystal structure of PCBM and the efficiency of MDMO-PPV:PCBM "plastic" solar cells. *Chem. Commun.* **2003**, *9*, 2116–2118.

(13) Chu, C.-W.; Yang, H.; Hou, W.-J.; Huang, J.; Li, G.; Yang, Y. Control of the Nanoscale Crystallinity and Phase Separation in Polymer Solar Cells. *Appl. Phys. Lett.* **2008**, *92*, 103306–103309.

(14) (a) Chirvase, D.; et al. Influence of Nanomorphology on the Photovoltaic Action of Polymer−fullerene Composites. *Nanotechnology* **2004**, *15*, 1317. (b) Treat, N. D.; Brady, M. A.; Smith, G.; Toney, M. F.; Kramer, E. J.; Hawker, C. J.; Chabinyc, M. L. Interdiffusion of PCBM and P3HT Reveals Miscibility in a Photovoltaically Active Blend. *Adv. Energy Mater.* **2011**, *1*, 82–89.

(15) Inoue, K.; Ulbricht, R.; Madakasira, P. C.; Sampson, W. M.; Lee, S.; Gutierrez, J.; Ferraris, J.; Zakhidov, A. A. Temperature and Time Dependence of Heat Treatment of RR-P3HT:PCBM Solar Cell. *Synth. Met.* **2005**, *154*, 41–44.

(16) (a) Padinger, F.; Rittberger, R.; Sariciftci, N. Effects of Postproduction Treatment on Plastic Solar Cells. *Adv. Funct. Mater.* **2003**, *13*, 85–88. (b) Müller, C.; Ferenczi, T. A. M.; Campoy-Quiles, M.; Frost, J. M.; Bradley, D. D. C.; Smith, P.; Stingelin-Stutzmann, N.; Nelson, J. Binary Organic Photovoltaic Blends: A Simple Rationale for Optimum Compositions. *Adv. Mater.* **2008**, *20*, 3510–3515.

(17) (a) Kim, Y.; Cook, S.; Tuladhar, S. M.; Choulis, S. A.; Nelson, J.; Durrant, J. R.; Bradley, D. D. C.; Giles, M.; McCulloch, I.; Ha, C.-S.; Ree, M. A Strong Regioregularity Effect in Self-Organizing Conjugated Polymer Films and High-Efficiency Polythiophene:Fullerene Solar Cells. *Nat. Mater.* **2006**, *5*, 197–203. (b) Chiu, M.-Y.; Jeng, U.-S.; Su, C.-H.; Liang, K. S.; Wei, K.-H. Simultaneous Use of Small- and Wide-Angle X-ray Techniques to Analyze Nanometerscale Phase Separation in Polymer Heterojunction Solar Cells. *Adv. Mater.* **2008**, *20*, 2573–2578. (c) Kim, J. Y.; Frisbie, C. D. Correlation of Phase Behavior and Charge Transport in Conjugated Polymer/Fullerene Blends. *J. Phys. Chem. C* **2008**, *112*, 17726–17736. (d) Baek, W.-H.; Yang, H.; Yoon, T.-S.; Kang, C. J.; Lee, H. H.; Kim, Y.-S. Effect of P3HT:PCBM Concentration in Solvent on Performances of Organic Solar Cells. *Sol. Energy Mater. Sol. Cells* **2009**, *93*, 1263–1267. (e) Shin, M.; Kim, H.; Park, J.; Nam, S.; Heo, K.; Ree, M.; Ha, C.-S.; Kim, Y. Abrupt Morphology Change upon Thermal Annealing in Poly(3-Hexylthiophene)/Soluble Fullerene Blend Films for Polymer Solar Cells. *Adv. Funct. Mater.* **2010**, *20*, 748–754. (f) Keivanidis, P. E.; Clarke, T. M.; Lilliu, S.; Agostinelli, T.; Macdonald, J. E.; Durrant, J. R.; Bradley, D. D. C.; Nelson, J. Dependence of Charge Separation Efficiency on Film Microstructure in Poly(3-hexylthiophene-2,5-diyl):[6,6]-Phenyl-C61 Butyric Acid Methyl Ester Blend Films. *J. Phys. Chem. Lett.* **2010**, *1*, 734–738. (g) Nam, S.; Shin, M.; Kim, H.; Kim, Y. Temperature/Time-Dependent Crystallization of Polythiophene:Fullerene Bulk Heterojunction Films for

Polymer Solar Cells. *Nanoscale* **2010**, *2*, 2384–2389. (h) Kim, H. J.; Park, J. H.; Lee, H. H.; Lee, D. R.; Kim, J.-J. The Effect of Al Electrodes on the Nanostructure of Poly(3-hexylthiophene): Fullerene Solar Cell Blends during Thermal Annealing. *Org. Electron.* **2009**, *10*, 1505–1510. (i) Kim, H. J.; Lee, H. H.; Kim, J.-J. Real Time Investigation of the Interface between a P3HT:PCBM Layer and an Al Electrode during Thermal Annealing. *Macromol. Rapid Commun.* **2009**, *30*, 1269–1273. (j) Wang, T.; Dunbar, A. D. F.; Staniec, P. A.; Pearson, A. J.; Hopkinson, P. E.; MacDonald, J. E.; Lilliu, S.; Pizzey, C.; Terrill, N. J.; Donald, A. M.; Ryan, A. J.; Jones, R. A. L.; Lidzey, D. G. The Development of Nanoscale Morphology in Polymer:Fullerene Photovoltaic Blends during Solvent Casting. *Soft Matter* **2010**, *6*, 4128–4134. (k) Agostinelli, T.; Lilliu, S.; Labram, J. G.; Campoy-Quiles, M.; Hampton, M.; Pires, E.; Rawle, J.; Bikondoa, O.; Bradley, D. C. D.; Anthopoulos, T. D.; Nelson, J.; Macdonald, J. E. Real Time Investigation of Crystallization and Phase Segregation Dynamics in P3HT/PCBM Solar Cells during Thermal Annealing. *Adv. Funct. Mater.* **2011**, DOI 10.1002/adfm.201002076.

(18) Kiel, J. W.; Kirby, B. J.; Majkrzak, C. F.; Maranville, B. B.; Mackay, M. E. Nanoparticle Concentration Profile in Polymer-Based Solar Cells. *Soft Matter* **2010**, *6*, 641–646.

(19) (a) Toney, M. F.; Brennan, S. Observation of the Effect of Refraction on X-rays Diffracted in a Grazing-Incidence Asymmetric Bragg Geometry. *Phys. Rev. B* **1989**, *39*, 7963. (b) Wolff, M.; Magerl, A.; Zabel, H. Structure of Polymer Micelles at the Solid Interface. *Phys. B* **2005**, *357*, 84–87.

(20) Kim, Y.; Nelson, J.; Durrant, J. R.; Bradley, D. D. C.; Heo, K.; Park, J.; Kim, H.; McCulloch, I.; Heeney, M.; Ree, M.; Ha, C.-S. Polymer Chain/Nanocrystal Ordering in Thin Films of Regioregular Poly (3-hexylthiophene) and Blends with a Soluble Fullerene. *Soft Matter* **2007**, *3*, 117–121.

(21) Pingree, L. S. C.; Reid, O. G.; Ginger, D. S. Imaging the Evolution of Nanoscale Photocurrent Collection and Transport Networks during Annealing of Polythiophene/Fullerene Solar Cells. *Nano Lett.* **2009**, *9*, 2946–2952.

(22) Yang, H.; LeFevre, S. W.; Ryu, C. Y.; Bao, Z. Solubility-Driven Thin Film Structures of Regioregular Poly(3-hexyl thiophene) Using Volatile Solvents. *Appl. Phys. Lett.* **2007**, *90*, 172116–3.

(23) Noma, T.; Takada, K.; A., L. Surface-Sensitive X-ray Fluorescence and Diffraction Analysis with Grazing-Exit Geometry. *X-ray Spectrom.* **1999**, *28*, 433–439.

(24) Werzer, O.; Matoy, K.; Strohriegl, P.; Resel, R. Temperature Treatment of Semiconducting Polymers: An X-ray Reflectivity Study. *Thin Solid Films* **2007**, *515*, 5601–5605.

(25) *MATLAB: Matlab User Guide*.

(26) Wu, T.-M.; Blackwell, J.; Chvalun, S. N. Determination of the Axial Correlation Lengths and Paracrystalline Distortion for Aromatic Copolyimides of Random Monomer Sequence. *Macromolecules* **1995**, *28*, 7349–7354.

(27) (a) Hosemann, R. Röntgeninterferenzen an Stoffen mit flüssigkeitsstatistischen Gitterstörungen. *Z. Phys.* **1950**, *128*, 465–492. (b) Hosemann, R. H.; Hindeleh, A. M. Structure of crystalline and paracrystalline condensed matter. *J. Macromol. Sci. Phys.* **1995**, *B34*, 327–356.

(28) Kanai, K.; Miyazaki, T.; Suzuki, H.; Inaba, M.; Ouchi, Y.; Seki, K. Effect of Annealing on the Electronic Structure of Poly(3-hexylthiophene) Thin Film. *Phys. Chem. Chem. Phys.* **2010**, *12*, 273–282.

(29) Dorf, R. C.; Bishop, R. H. *Modern Control Systems*, 11th ed.; Pearson Prentice Hall: London, 2008.

(30) Wypych, G. *Handbook of Plasticizers*; ChemTee Publishing: Toronto, 2004.

(31) Jang, J.; Lee, D. K. Plasticizer effect on the melting and crystallization behavior of polyvinyl alcohol. *Polymer* **2003**, *44*, 8139–8146.

(32) Birkholz, M. *Thin Film Analysis by X-Ray Scattering*; Wiley-VCH: Weinheim, Germany, 2005.

(33) Kiel, J. W.; Eberle, A. P. R.; Mackay, M. E. Nanoparticle Agglomeration in Polymer-Based Solar Cells. *Phys. Rev. Lett.* **2010**, *105*, 168701.

(34) Campoy-Quiles, M.; Ferenczi, T.; Agostinelli, T.; Etchegoin, P. G.; Kim, Y.; Anthopoulos, T. D.; Stavrinou, P. N.; Bradley, D. D. C.; Nelson, J. Morphology Evolution via Self-Organization and Lateral and Vertical Diffusion in Polymer:Fullerene Solar Cell Blends. *Nat. Mater.* **2008**, *7*, 158–164.